Astron. Astrophys. 351, 860–868 (1999)

ASTRONOMY AND ASTROPHYSICS

BVRI-Hα surface photometry of peculiar ring galaxies*

I. HRG 2302

M.L.M. Myrrha[1], **L.P.R. Vaz**[1], **M. Faúndez-Abans**[2], **M. de Oliveira-Abans**[2], **and D.S.L. Soares**[1]

[1] Departamento de Física, ICEX–UFMG, C.P. 702, 30.123-970 Belo Horizonte, MG, Brazil
[2] CNPq/Laboratório Nacional de Astrofísica, C.P. 21, 37.500-000, Itajubá, MG, Brazil
(leticia@fisica.ufmg.br, lpv@fisica.ufmg.br, mfaundez@lna.br, mabans@lna.br, dsoares@fisica.ufmg.br)

Received 11 February 1999 / Accepted 22 September 1999

Abstract. Detailed BVRI-Hα photometry has been obtained for the ring galaxy HRG 2302. This is probably a still interacting system which shows two principal components: the target, which is a knotted ringed-disk, and the intruder, an elongated galaxy with two substructures probably caused by the interaction. The existence of H II emission regions is suggested by Hα images and medium dispersion spectra of the three brightest parts of this system. Analysis of a color-color diagram suggests recent star formation, in agreement with the behavior of interacting galaxies with nuclear emission. HRG 2302 has been previously classified as a Polar Ring galaxy (Faúndez-Abans & de Oliveira-Abans 1998a), but we have reclassified it as Elliptical-Knotted, based on the morphological substructures found. This work reveals, for the first time, the existence of at least 15 fainter galaxies in the field within $\sim 4'$ around HRG 2302, giving positions and integrated standard magnitudes for all of them.

Key words: galaxies: formation – galaxies: individual: HRG 2302 – galaxies: interactions – galaxies: peculiar – galaxies: structure

1. Introduction

Among the peculiar galaxies, there are objects which take on the appearance of a smoky ring. These beautiful objects, generically called Ring Galaxies, can be classified into Normal Ring Galaxies (NRG) and *peculiar Ring Galaxies* (pRG[1]). Among the NRG we find objects with morphology SB and Sa and no evidence of interaction with other objects. They are formed through resonances in stellar orbits and dust and gas flows, due to the presence of a bar or an oval distortion in the galactic gravitational potential (e.g., Buta 1995 and references therein). The pRG classification, in turn, is used for objects with distorted structures, off-center nuclei, and other aspects that may be the result of events such as collision, merging and tidal interaction. A description of the morphological characteristics of the pRGs is found in Faúndez-Abans & de Oliveira-Abans (1998a, hereafter FAOA). Another point in studying pRGs is that they are useful tools in the study of star formation in interacting systems. Models indicate that the ring forms when another galaxy, the intruder, collides almost head-on with a larger rotating disk galaxy, the target (Lynds & Toomre 1976, Theys & Spiegel 1977, Bekki 1997, 1998). It must be pointed out that the intruder can be part of the ring galaxy itself, as is the case in PRGs, or it can be in the close neighborhood.

Studies in the last decade have shown that the gravitational interaction is the most important factor in galactic evolution and affects directly properties such as size, morphological type, luminosity, star formation rate, and mass distribution. The perturbation in the gravitational potential of the target galaxy produces radially expanding density waves, which propagate outward from the nucleus and trigger the birth of stars. Thus, star formation history is preserved in the radial color distribution of the material between the rings. Discussions on general properties of Ring Galaxies can be found in Theys & Spiegel (1976, 1977), Lynds & Toomre (1976), Toomre (1978), Appleton & Struck-Marcell (1996); for a review, see Dennefeld & Materne (1980).

This is the first of a series of papers on detailed analysis of a sample of pRGs, based on new photometric (BVRI-Hα) and medium dispersion spectroscopic measurements of the ring galaxy components and their nearest neighbors. The pRGs selected here are studied as detailed as possible with medium

Table 1. Data for known sources within $10'$ around HRG 2302: coordinates (J2000), distance in arc minutes from HRG 2302, the logarithm of the flux (mJ) at 4.85 GHz, and the extinction in the B band, according to NED.

source	α_{2000} h m s	δ_{2000} ° ′ ″	dist ′	$\log F$ (mJ)	ext
PMN J1634-8058	16 34 48.79	−81 58 19.6	9.0	1.82	0.47
PMNM 162428.3-810826	16 33 39.98	−81 14 53.6	9.6	1.41	0.46

Send offprint requests to: M.L.M. Myrrha

* Based on observations made at the Observatório do Pico dos Dias (OPD), operated by the MCT/CNPq/Laboratório Nacional de Astrofísica, in the state of Minas Gerais, Brazil

[1] Note that PRG (all uppercase letters) is normally used to denominate Polar Ring Galaxies, as, e.g., in Whitmore et al. 1990, Reshetnikov et al. 1994, 1995, 1996, Bekki 1997, 1998 and others. Many indications suggest that most PRGs are pRGs

($\lesssim$1.5 m class) size telescopes. At the same time we are also searching for adequate candidates for further studies. Among our aims are the clear identification of the target and intruder components of the system, their morphological classification, and to infer the system's dust and gas content. Such an investigation is important for providing constraints and input parameters for numerical simulations and analytical modeling of pRGs (Bekki 1998, Athanassoula et al. 1997).

1.1. Early data on HRG 2302

HRG 2302 has been selected from the recent classification work by FAOA, which is concerned with the morphology of pRGs. HRG stands for Hertling Ring Galaxy, using the nomenclature of Faúndez-Abans et al. (1992). The digits are composed by the SRC/ESO plate number multiplied by 100 plus the ring galaxy number in order of appearance on that plate for increasing right ascensions.

The morphological classification of HRG 2302 according to the NASA/IPAC Extragalactic Database (NED) is elliptical, while FAOA classify it as a PRG. The extinction in the B band is 0.47 mag (NED) and the galaxy is located near the Galactic plane ($l = 310\overset{\circ}{.}81$ and $b = -21\overset{\circ}{.}84$).

Little is known about HRG 2302 and its neighborhood. Only the 2 radio sources given in Table 1 were found in a search for other objects within $10'$ around it in the NED database. The images reveal, however, the existence of 15 probable non-stellar objects inside a region of $4'$-radius around HRG 2302, as shown in Fig. 1. These objects have been identified through the comparison of their profiles with the image PSF, from which they deviate systematically in all frames. They were assigned the letters A to O, in order of increasing right ascension; their coordinates and integrated standard magnitudes are given in Table 2. Curiously, not even the bright cigar-like galaxy on the northeast ("M"), clearly visible in the ESO Digitalized Sky Survey plates, has an entry in NED, so far.

The photometric analysis presented herein is based on a set of 13 CCD images taken through standard BVRI-Hα filters. The spectroscopic analysis is based on 2 medium dispersion (CCD) spectra covering 216 nm and centered at $\sim$600 nm.

Sect. 2 describes the photometric observations and the data reduction process. The global photometric properties are presented in Sect. 3, together with the morphological structure of the object. Preliminary spectroscopic data and their interpretation are presented in Sect. 4. The results are discussed in Sect. 5, and the conclusions are presented in Sect. 6. A detailed description of the galaxies in the field of HRG 2302 will be given elsewhere.

2. Photometric observations and data reduction

The photometric observations were obtained in August, 1994, on the 1.6 m telescope of the OPD (LNA/CNPq), Brazil, equipped with direct imaging camera #1 (details in `http://www.lna.br/instrum/camara/camara.html`) and an EEV 770×1152 22.5 μm square pixels CCD-05-20-0-202 detector #048 (thick, front-illuminated and coated for the UV). The readout noise was 11.55 e^- and the gain 10.05 e^-/ADU. The photometric BVRI bands are defined as in Bessel (1990) and given in the URL above, together with the detector quantum efficiency. The Hα interference filter used has the central wavelength at 670.7 nm and a FWHM of 10.7 nm. The plate scale is $0\overset{''}{.}30$/pix.

Table 2. Coordinates of the centroids (J2000, calculated differentially from the centroid of HRG 2302) and integrated standard BVRI magnitudes for HRG 2302 and the 15 objects of Fig. 1. The estimated error in the determination of the centroid position differences is <1 pixel ($\lesssim 0\overset{''}{.}3$ at our plate scale). However, we adopt a conservative estimate of $\pm 1''$ ($\pm 0\overset{s}{.}1$) for the error in the positions of the objects from A to M. The coordinates of HRG 2302 were taken from NED.

object	α_{2000} h m s	δ_{2000} ° ′ ″	B	V	R	I
2302	16 32 35.69	−81 05 39.7	16.41 ±20	15.685 ±92	15.201 ±76	14.56 ±22
A	16 32 05.3	−81 05 41	22.07 ±96	22.46 ±72	20.78 ±21	19.82 ±37
B	16 32 08.5	−81 03 53	20.30 ±25	20.00 ±12	19.513 ±96	18.63 ±25
C	16 32 11.6	−81 05 00	22.43 ±69	19.97 ±12	19.379 ±92	18.40 ±24
D	16 32 16.8	−81 06 30	21.97 ±60	20.83 ±19	19.94 ±12	18.94 ±26
E	16 32 19.2	−81 06 03	20.98 ±40	21.56 ±32	20.52 ±17	20.73 ±93
F	16 32 25.5	−81 06 46	23.6 ±1.7	22.57 ±47	21.25 ±18	19.35 ±26
G	16 32 30.1	−81 06 54	22.57 ±84	21.19 ±23	20.47 ±15	20.57 ±70
H	16 32 38.4	−81 06 48	19.40 ±20	18.695 ±95	18.026 ±78	17.56 ±23
I	16 32 43.1	−81 06 41	19.74 ±21	18.296 ±95	17.590 ±77	16.80 ±23
J	16 32 50.2	−81 05 58	20.19 ±22	18.209 ±96	17.430 ±77	16.57 ±23
K	16 32 50.6	−81 04 59	20.30 ±34	21.92 ±43	20.70 ±18	18.48 ±26
L	16 32 55.5	−81 05 19	20.46 ±25	19.46 ±10	18.850 ±82	18.26 ±24
M	16 33 03.2	−81 04 52	17.92 ±19	17.205 ±92	16.739 ±76	16.14 ±23
N	16 33 08.8	−81 04 01	23.29 ±67	22.38 ±22	21.78 ±14	20.25 ±27
O	16 33 09.5	−81 04 04	22.99 ±46	21.46 ±13	20.930 ±95	19.89 ±25

2.1. Data reduction

CCD image processing and data analysis have been done using standard procedures, IRAF and STSDAS. Photometric standard stars from Landolt (1992) were observed and the calibration to the standard BVRI photometric system was performed in the usual way (see e.g. Reshetnikov et al. 1994), the quality of which may be inferred by the data of Table 3. The seeing during the observations was $< 2''$. The sky brightness, in mag arcsec^{-2} for the BVRI filters, was 21.73, 20.53, 19.89 and 18.25, respectively.

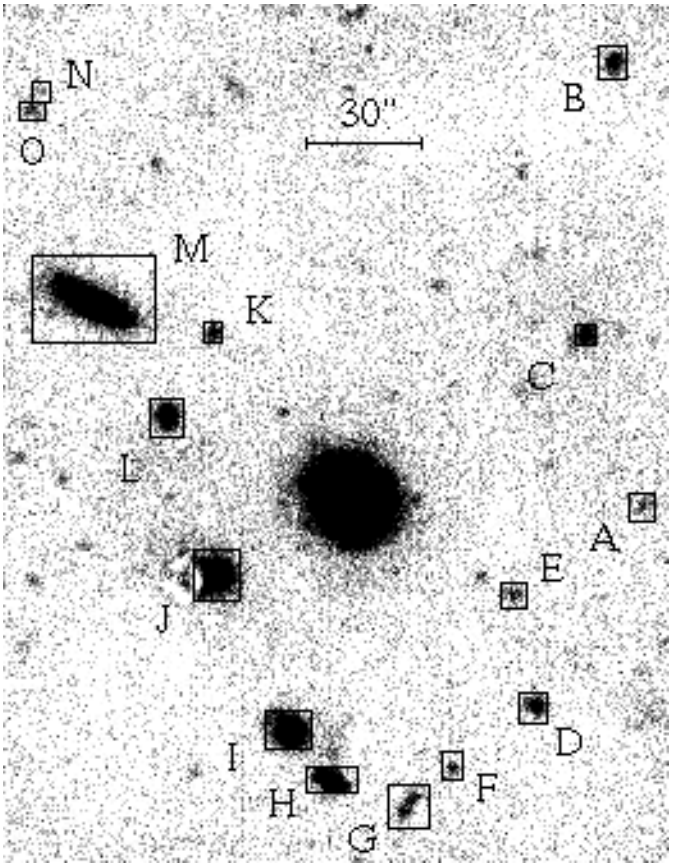

Fig. 1. The field around HRG 2302 in the R filter (logarithmic scale). Using IRAF standard tools all identified stars have been removed with the frame's most representative point spread function (PSF). In this and in Figs. 2 to 3 North is up and East to the left. The "doughnut" to the left of object J is caused by dust particles near the focal plane of the instrument (see e.g. Gullixson 1992). It is not present on the other frames, where this object's profile also deviates from the stellar one.

Table 3. Standard deviation (σ) for the calibration to the standard BVRI system for each night observed in 1994, together with the number of standard stars used in the process (N).

	Aug 05	Aug 06	Aug 07	Aug 08
$\sigma_{\rm B}$ (N)	0.059 (15)	0.035 (22)	0.027 (18)	0.065 (8)
$\sigma_{\rm V}$ (N)	0.025 (12)	0.058 (19)	0.037 (18)	0.066 (8)
$\sigma_{\rm R}$ (N)	0.020 (12)	0.058 (23)	0.042 (18)	0.046 (8)
$\sigma_{\rm I}$ (N)	0.052 (12)	0.056 (22)	0.059 (18)	0.042 (8)

The PSF was determined based on more than 20 reasonably bright and isolated stars on each frame. The removal of foreground stars achieved with the IRAF task ALLSTAR was better than the results obtained with PEAK/SUBSTAR. In this process, at least 15 candidate non-stellar objects, shown in Fig. 1, have been found. Their profiles are larger than and different from the profiles of the stellar objects, including those with similar magnitude in the same frame.

The sky background has been estimated in two different ways: (1) by examining the median count in concentric rings of different widths centered at the galaxy with the external radius extending to the limits of the frame (more than 5 times the visual radius of HRG 2302 from its center), and estimating the lowest intensity level; (2) by fitting the sky background with a bidimensional third order spline with 1 to 4 pieces in both dimensions, depending on the frame. All the residual stars (not completely removed by the PSF), blemishes, and the objects visible in Fig. 1 were isolated from the calculations of the sky fitting surface by use of rectangular masks. The typical uncertainty of the background level is (0.5 -1)%. We noticed that the longer the wavelength being imaged the larger the number of spline pieces for a reasonable sky fitting surface.

3. Image enhancement

To extract as much information as possible from the images, we have applied the techniques of image enhancement by transform processing described in Faúndez-Abans & de Oliveira-Abans (1998b), with emphasis on the R and I frames due to their better S/N ratio.

3.1. Image transforming

In order to enhance high-frequency features, a high-pass filter from the work cited above has been applied to the R image of HRG 2302. Five features can be discerned in Fig. 2: a central bulge, an extended faint background nebulosity, an apparently knotted ring, and two large knots (one on the SE and another on the SW of the bulge).

The central region shows a filamentary structure extending from the nuclear part of the central bulge in the SW direction, along its major axis. This has been confirmed in Fourier-hologram experiments.

The residuals of the subtraction of median-filtered R and I frames (with a 20×20-pix or $6\farcs0\times6\farcs0$ kernel) from the original ones (Fig. 3) highlight the knotty ring and the elongated nature of the central bulge. The knot III is bright in both filters and could be composed of two clumps, as opposed to the other knots (see the panel for the I image in Fig. 3).

This technique of subtracting blurred masks has been applied to the Hα image. Median and gaussian filters have been used, both with kernels of 20×20 pix. The result for the median filter is displayed in Fig. 3. The ionized gas is concentrated in the knots and in regions I and II. They are probable sites of induced star formation. Discriminating the filamentary structure of the feature II is straightforward, as shown in Fig. 3. The structure of HRG 2302 resembles, in part, the galaxy NGC 985 – an object which is more consistent with a tightly wrapped one-armed spiral plus a linear bar-like structure (see Appleton & Marcum 1993; more on NGC 985 in, e.g., Appleton & Struck-Marcell 1987, Rodríguez Espinosa & Stanga 1990, Appleton & Marston 1997, and Bransford et al. 1998). On the other hand, based on this work's data we discern four principal structures in HRG 2302: a central bulge, an elongated structure extending from the nuclear region along the SW direction, a prominent knot on the apparent ring, and the "ring" itself, composed by several fainter knots.

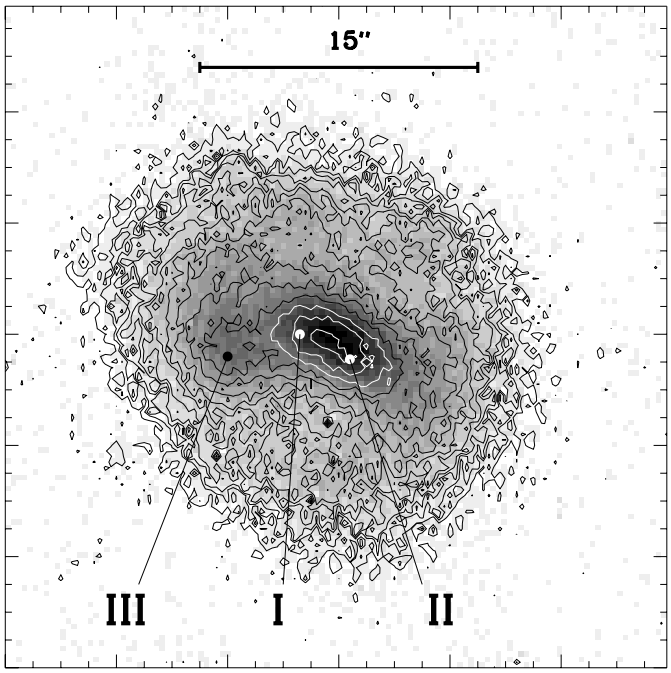

Fig. 2. High-pass filtering of the R image of HRG 2302 (intensity scale), with the perturbed isophotes of the central region of the bulge (R standard magnitudes) overlaid as contour levels (separated by $0\overset{\mathrm{m}}{.}2$). The central bulge and material around the probable lumpy ring have been enhanced by the filtering technique. A filamentary structure connected to the nuclear region extends along the SW direction. The roman numbers I and II designate, respectively, the nuclear region and the filament which form together the bulge. The number III designates the SE bright ring knot (see Sect. 4).

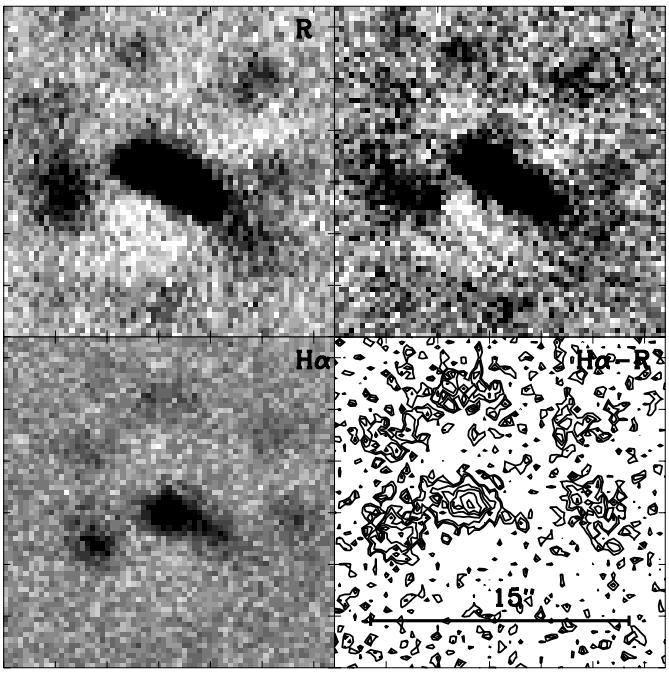

Fig. 3. In the upper left, upper right and lower left panels we show the residual images of the median-filtered frames subtracted from the original data for the R, I and Hα filters, respectively. In these panels the lighter areas are artifacts introduced by the method. In the lower right panel we show the Hα continuum-subtracted isophote map (Hα − R, intensity scale) of HRG 2302. The isophotal levels are arbitrary.

The filamentary structure mentioned above can also be seen in the isophotal contour Hα map shown in Fig. 3. We subtracted the R image from the Hα frame, as an approximation for the continuum correction. It can be seen that the features revealed in Fig. 3 are consistent in all panels. However, these figures show, also, that not all nodules or condensations are Hα emitters.

3.2. Image modeling

Isophotal analysis and modeling of HRG 2302 were performed through the STSDAS tasks ELLIPSE and a modified version of BMODEL, adapted for Ring Galaxies.

To a greater or lesser extent, all the knots revealed in this study are present in the B, V, R, and I frames. The bright knot on the SE (region III) is prominent in all passbands and there are hints, mainly in the redder images, that it might be composite, confirming the results of Sect. 3.1.

3.3. Light and structural parameter profiles

3.3.1. Luminosity and color profiles

Fig. 4 shows the luminosity profiles (LP) of HRG 2302 along the mean (both major and minor) axes of the isophotal ellipses of its central bulge. The isophotal centers and the directions of the axes obtained with the STSDAS task ELLIPSE for all the colors were averaged to find the mean major and minor axes. The LP for the calibrated BVRI passbands are shown in 3 different ways, while the LP for the Hα filter is shown for the observations only and with an arbitrary zero point. Firstly, we show the LP obtained directly from the calibrated images. Secondly, the BVRI LP obtained from the model generated in Sect 3.2 are traced. These LP are shown as curves with lines of different styles and thickness. Lastly, we show (as points with different symbols) the equivalent LP for the BVRI passbands, defined as the elliptical isophotal magnitude level as a function of the radius of the circle which has the same area as the ellipse (the equivalent radius, see de Vaucouleurs 1948). The equivalent LP along the major and minor axes are the same for each passband and are shown in the panels of Fig. 4, folded around the centroid of the galaxy.

The model fits the observations well in the central part of the galaxy ($-6'' \lesssim R \lesssim 4''$: major axis; $-3'' \lesssim R \lesssim 3''$: minor axis). The equivalent LP does represent a mean between the values along the major and the minor axes, and as such the equivalent LP tends to ignore local deviations due to nodules, condensations and similar substructures.

Notice that the mean centroid of the BVRI maps, used in derivating the LP of Fig. 4, does not coincide with the centroid of the Hα image, which is displaced $\sim 1''\!.5$ to the NE. This can be clearly seen in the Hα LP along the semi–major axis, shown in Fig. 4. The effect in the centroid is caused by strong emission

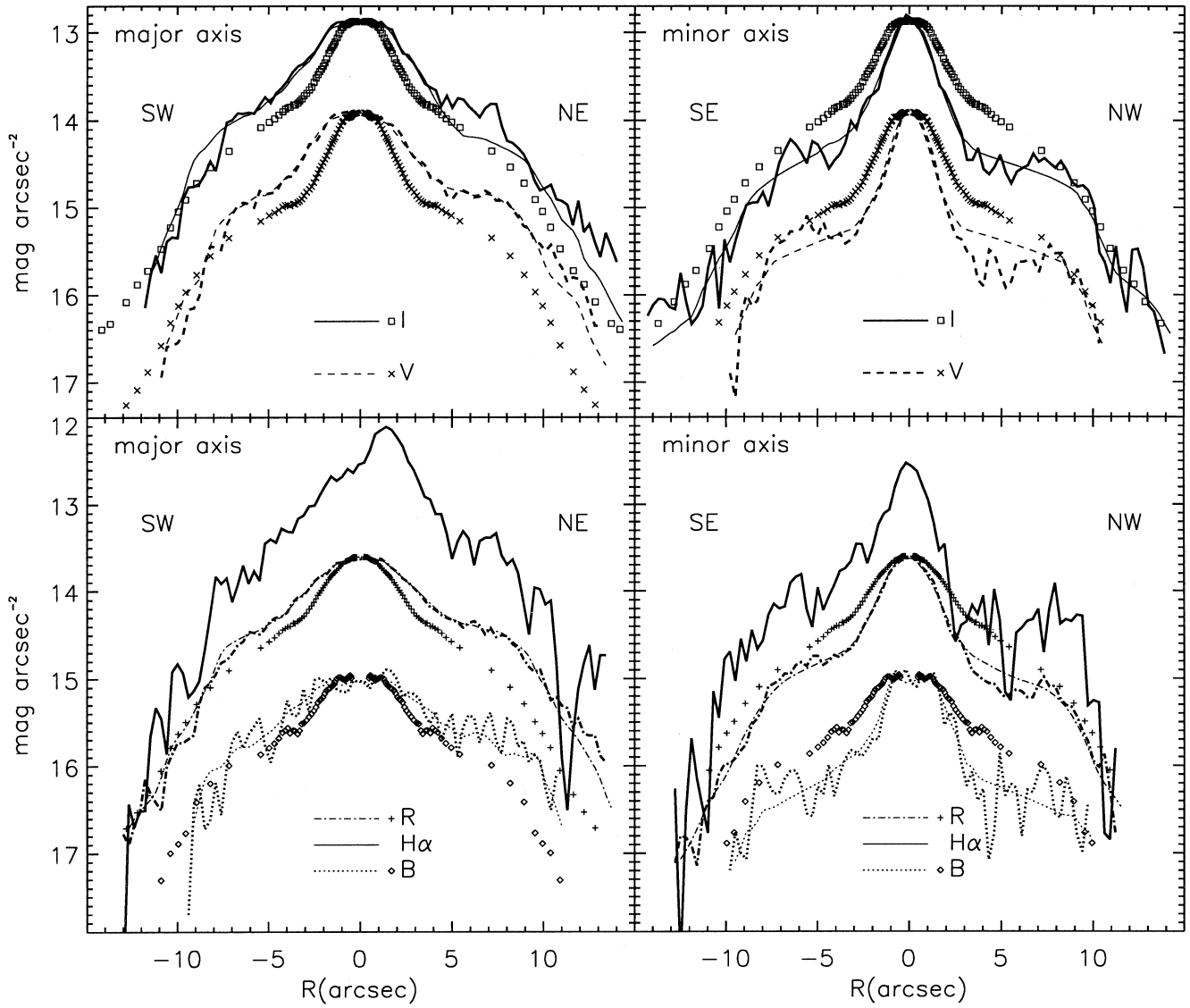

Fig. 4. Luminosity profiles in the BVRI passbands (standard magnitudes arcsec^{-2}) and for the Hα filter (magnitudes arcsec^{-2} with arbitrary zero point) vs. radius in arcseconds of the observations (thick lines) and models (thin lines) for HRG 2302. The BVRIHα passbands are represented with different line styles: B, R, Hα (lower panels), V and I (upper panels) along the major (left panels) and minor (right panels) axes. The equivalent profiles for the BVRI passbands are also shown, with different symbols for the B ($\diamond$) V ($\times$) R ($+$) I ($\Box$) passbands, reflected around the centroid of the galaxy (see Table 2).

from the clump located in the direction of the galaxy major axis, see Fig. 3, and obscuration by dust.

The color profiles of HRG 2302, as the calibrated color indices B$-$V, V$-$R and R$-$I along both mean axes, are shown in Fig. 5. The central region with a radius of $\sim 5''$ differs from the rest of the galaxy, showing redder B$-$V and R$-$I, but slightly bluer V$-$R indices, compared with the ring. We identify this central part as being the intruder in this interaction.

3.3.2. Structural parameter profiles

The central part, identified with the intruder, is well fit by ellipses with approximately constant ellipticity ($\epsilon \sim 0.6$) up to the semi-major axis of around $9''$. From this radius, which we identify as the upper limit for the intruder radius (regions I and II, Sect. 3.1), the ellipses become abruptly nearly circular ($\epsilon \sim 0.1$) in all passbands. In the inner part ($R \lesssim 3''$) there is an oscillation in the ellipticity, probably real, because it is present in all passbands, but possibly strongly influenced by the seeing conditions. The position angle and the B4 coefficient (the cos$(4E)$ term) follow the pattern, showing oscillations in this inner region, too. On the other hand, the position angle does not show the abrupt change at $R \sim 9''$ and remains approximately constant ($\approx 60^\circ$), presenting a slight systematic decrease as the semi-major axis increase.

The B4 coefficients for the B, V, and R images show similar behavior, not deviating much from zero albeit with predominance of negative values. This indicates a preference for a

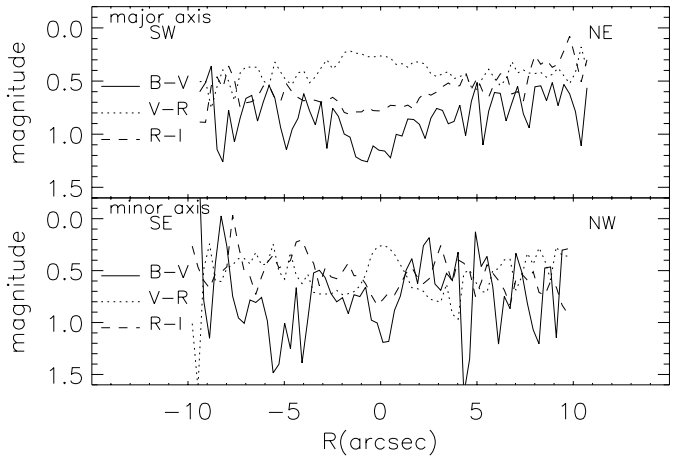

Fig. 5. Color profiles (standard magnitudes) B−V, V−R and R−I vs. radius in arcseconds of HRG 2302.

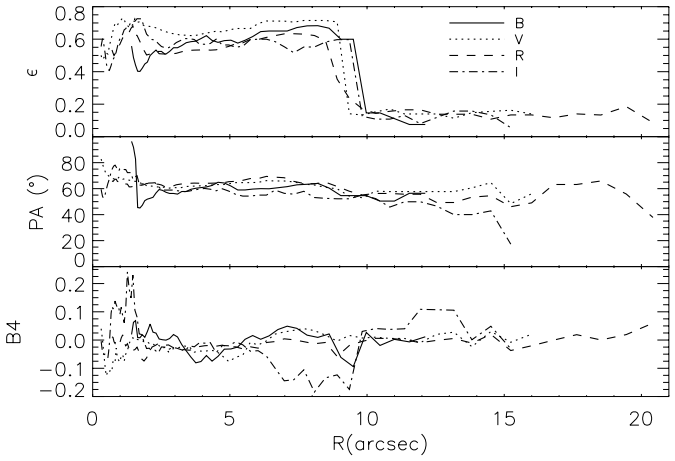

Fig. 6. Isophotal parameters of HRG 2302: ellipticity, position angles (in degrees, eastwards from the North) and the Fourier coefficient of the cos(4E) term (E is the ellipse eccentric anomaly), B4, versus the semi–major axis in arcseconds.

"boxy" shape in most of $a \lesssim 10''$. The behavior in the I color is different, showing larger negative values. This is probably due to the relatively poor quality of the I images, as this tendence is not evident in the other colors.

4. Preliminary spectroscopy

Spectroscopic observations were performed with the 1.6m-telescope at the OPD in August 26, 1998, equipped with a Cassegrain spectrograph and CCD #106 (1024×1024 square pixels, 24 μm each), with 4.1e^- readout noise and 5.0 e^-/ADU gain. The grating of 600 lines/mm was centered at 600 nm (dispersion of 84.1Å/mm and resolution of 2.0 pixels FWHM). Two spectra (20 min each) were obtained. The 3″ slit covered the brightest region of the galaxy. The slit was aligned with the EW direction in order to include the probable signatures of the intruder (regions I and II, see Fig. 2) and the target galaxy (region III).

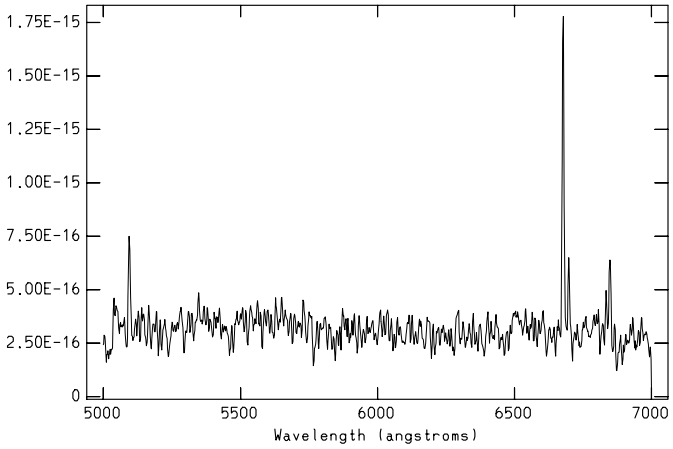

Fig. 7. Spectrum of the most prominent part of the intruder, region I, smoothed by a kernel of 3 pix. The vertical axis is the calibrated flux in units of erg s^{-1} cm^{-2} Å^{-1}.

Table 4. Preliminary parameters from the spectrum

Parameter	Regions		
	I	II	III
$\lambda\lambda$(6716/6731)	0.96	0.43	0.75
N_e(cm^{-1})	700	10,100	1,500
T_e(K)	20,500	–	–

The stars used for extinction and flux calibrations are tertiary standards from Baldwin & Stone (1984), as revised by Hamuy et al. (1992, see also Hamuy et al. 1994). The spectrum reduction has been done according to standard procedures employing IRAF.

A velocity of 5 996±21 km s^{-1} for the region I has been computed (z ∼ 0.020). Within the errors, the spectra of the three regions are not significantly shifted with respect to each other. Whether region I suffers a slow braking and this scenario is a result of a polar collision (see, e.g., Bekki 1998) remains yet to be confirmed by better resolution spectroscopic observations, a project now in progress. The three regions exhibit H II-region emission-type spectra with strong Hα, [N II], [S II] and [O III] emission lines (see Fig. 7).

The enhanced images of region III show clumps which may be the origin of most of the emission lines from this region. Whether region III is the displaced bulge of an original disk galaxy that has been disrupted due to a collision or whether it is the most prominent H II region under formation on the ring, is a matter of further discussion.

An attempt to determine the electron density of the regions I, II, and III has been made using the [S II] $\lambda\lambda$ 6761/6731 ratio and the [N II] relation $\lambda\lambda$ (6548 + 6583/5755), as listed in Table 4. The lack of λ5755 in the spectra of both region II and III and of λ6548 in region II has not allowed an estimate of the electron temperature in these regions. As the Hβ line was out of the observed range, a similar estimation of chemical abundances has not been possible. Nevertheless, a preliminary lower limit for oxygen abundance of 12+log[O/H] ∼ 8.3 has been estimated

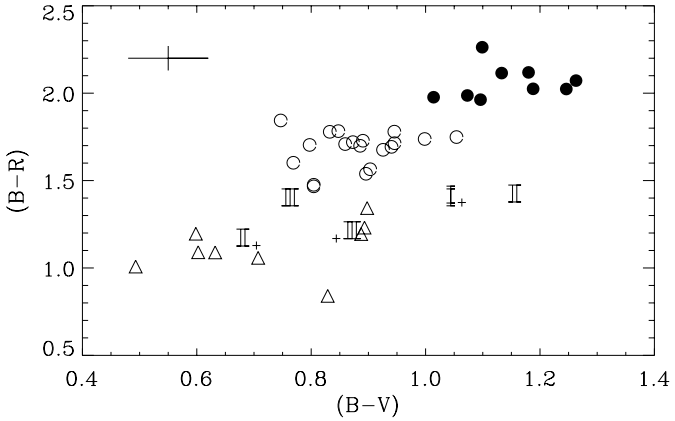

Fig. 8. Color-color diagram for HRG 2302 and HRG 54103. The filled and the open circles represent the nucleus and the ring of HRG 54103, respectively. The △ symbols represent the knots on HRG 2302's ring. Regions I, II and III are represented by these same letters; the ones without subscript represent the region of maximum intensity, which are the same for all filters; the ones with the subscript + represent regions of maximum color index as seen in the color maps. The 2σ (σ=0$^{\rm m}$.07) error bars in each axis are shown in the upper left part of the panel.

for region I (see also next section). Although being relatively low, this value is in agreement with recent oxygen abundance determinations from optical long-slit spectra of individual star-forming knots embedded in collisional rings by Bransford et al. (1998).

5. Discussion

The images of HRG 2302 have revealed a knotty ring around an elongated perturbed bulge. There are two prominent knots: the one located in region III and another, located to the SW, that has no significant emission in Hα. The bulge is composed by two substructures: a round compact one (region I) and a filament in the direction of the SW prominent knot (region II). If this object is a result of a galactic collision as, for example, in Lynds & Toomre (1976, Figs. 5 and 6), it seems reasonable to suggest that region III could be part of the target galaxy's tenuous bulge, which has been displaced during the encounter (the disk would have given rise to the ring), and that regions I and II together are part of the perturbed (disrupted?) projectile galaxy. The Hα image indicates the presence of bright H II regions in the central object as well as in some of the knots. These may be regions of induced star formation. On the other hand, there seems to be no obvious emission from the SW knot (see Fig. 3).

The B−R versus B−V diagram in Fig. 8 contains integrated photometry of selected 4×4-square pixel areas of the bulges and rings of HRG 2302 and HRG 54103. The latter (Faúndez-Abans et al. 1999) has been included for comparison and because it shows no evidence of interaction (Faúndez-Abans & de Oliveira-Abans 1998b), and has been cataloged as NRG by Buta (1995). Thus, a different behavior is to be expected when compared with an object which has probably undergone interaction. The average mean error in both colors is less than 0.07 mag. The measurements of regions I, II, and III are represented in Fig. 8 by these same numbers. The spot of maximum intensity in each region (represented with subscript +) does not, in general, coincide with that of larger color indices, that is, the brighter portions may not be the redder ones. Thus, two measurements per region have been made. No systematics is shown by these measurements except for the fact that all fall in the same B−R$<$ 1.5 region occupied by the ring knots. The ring is represented by open triangles and nine measurements have been made along its surface, on the most prominent clumps. The bulge and ring of HRG 54103 are represented by filled circles and open circles, respectively. An inspection of Fig. 8 shows that HRG 2302 is definitely bluer than HRG 54103. This may be caused by localized star formation, a result confirmed by this work's spectra, which resemble those of H II regions. The extreme II data point on the right corresponds to a spot that does not appear in Hα images; this is probably a neutral substructure superimposed on the blue filament.

The colors of the knots lie in the range $0.4 < (\mathrm{B-V}) < 0.9$, agreeing with early photoelectric measurements by Theys & Spiegel (1976). Evidences from the color profiles (Fig. 5) point to classifying the intruder as an early-type system. Both along the major and minor axes, R−I ranges from 0.5–0.7, within $5''$ from the center. These are typical early-type galaxy colors (see Poulain and Nieto 1994). Although rather noisy, the B−V color ranges from 0.8 to 1.1, also around the typical value of 1.0 found in elliptical and lenticular galaxies. V−R has overall values (0.2–0.5) that are systematically lower than those measured in early-type galaxies, which is likely the effect of dust extinction. The presence of dust is expected due to the disruption of the target galaxy, seemingly a gas-rich late-type system.

There seems to be a radial color gradient, a known property of ring galaxies. The regions inside the knots are generally redder both in B−V and B−R. These color changes are consistent with the simple starburst model in which the stars are formed in the ring and evolve in the wake of the ring causing the redder colors observed there (cf. Appleton & Struck-Marcell 1996). The global B−V color of the ring is 0.75 ± 0.15 (1σ), which is, within the errors, the same as the median B−V of 0.52 ± 0.10 found by Marston & Appleton (1995) for a sample of twelve northern ring galaxies. In order to know how large the influence of dust absorption in the radial color gradients is, one would require near-infrared observations of the system.

Plotting HRG 2302 in the line-ratios diagnostics diagram of forbidden-line strengths for interacting galaxy nuclei, from Keel et al. (1985), places it inside the sector defined by nuclear H II regions of interacting galaxies. The line-ratios obtained in the present work are: $\log([\mathrm{O\,III}]_{\lambda\,5007}/\mathrm{H}_\alpha) = -0.78$ and $\log([\mathrm{N\,II}]_{\lambda\,6584}/\mathrm{H}_\alpha) = -0.64$. Similarly, we estimate for the nuclear and disk Hα+[N II] emission equivalent widths the values: 63 mÅ for the central bulge (regions I and II) and 69 mÅ for region III. Plotting these numbers in Kennicutt et al.'s (1987) correlation diagram, places this pRG in the intersection of the areas defined by interacting and non-interacting galaxies, closer to the interacting one.

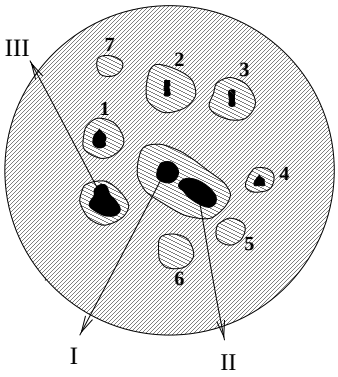

Fig. 9. Simplified sketch of HRG 2302. Black regions are Hα-emitters while dashed ones are only visible through broad-band filters. The circular dashed region represents the extended faint background nebulosity. In the suggested collisional model for the system, structures I and II form the intruder and III is the displaced nucleus of the target galaxy.

Fosbury & Hawarden (1977) estimated elemental abundances for two of the HII regions on the ring of A0035 (the "Cartwheel" galaxy) and found low metallicity values: 12 + log[O/H] = 8.10 and 7.96. This work's oxygen abundance of at least 8.3 is then in agreement with the above-mentioned estimates. The existence of induced star-forming in the perturbed intruder as well as in the target is thus well characterized.

One can estimate the recent global star formation rate (age $\lesssim 10^9$ yr) in HRG 2302 from the blue luminosity (Sandage 1986, Young et al. 1996). We get 3.10×10^9 $L_{\odot,B}$ from the data obtained here and $H_\circ = 69\,km\,s^{-1}\,Mpc^{-1}$ (Ferrarese et al. 1999), implying an overall star formation rate, normalized to unit area, of 1.83×10^{-8} $M_\odot\ yr^{-1}\ pc^{-2}$. This is approximately 5 times as large as the average rate for late-type galaxies (Buat et al. 1989, Elmegreen 1998).

5.1. Geometry and composition

With the results obtained in the present analysis it is possible to speculate on the geometry and the overall structure of HRG 2302. The main conclusions are represented in Fig. 9. With the adopted $H_\circ$, a distance of 86 ± 9 Mpc has been derived. Table 5 displays the various components' estimated major and minor axes; the associated errors are 1.5 pix, 0.45 arcsec, and 0.19 kpc.

5.2. Alternative scenarios

Two tentative scenarios might be added to the one already discussed in the text. The final discrimination amongst them will be delayed until detailed spectroscopic studies as well as full mapping in the near-infrared and radio bands are performed.

Firstly, the possibility of a nuclear bar is considered. HRG 2302 is a dwarf galaxy, with integrated blue magnitude of –18.3 (similar to the LMC, for example). Regions I and II constitute a slightly inclined bar; region II has a foreground counterpart behind region I being thereby obscured. The B4-coefficient profile is consistent with a bar morphology since it shows negative values in most of the region within $10''$. Near-infrared observations are likely to uncover the entire bar morphology. The system is then a very early SBaV galaxy with the tightly wound arms resembling a knotted ring. The peak of Hα emission in region I, which is the assumed galaxy nucleus, is consistent with what is expected from gas being driven to the center, as derived from barred galaxies modeling (e.g., Roberts et al. 1979, Sakamoto et al. 1999).

Secondly, the possibility of a moderately fast encounter between HRG 2302 and another galaxy is considered. We suggest here a small-scale version of what may be happening in the Cartwheel system according to the mechanism put forward by Higdon (1996). Based in HI observations of the system, he attributes to a third neighbor galaxy, named G3 and other than the two closest to the Cartwheel's disk, the responsibility for generating the peculiar morphology observed in the system. G3 is shown to be linked to the main galaxy by a broad HI plume, at least in one channel map, suggesting an earlier passage ($\approx$ 300 Myr-old) with a moderate relative velocity of about 200 km s^{-1} (see Higdon's Fig. 17). HRG 2302 forms with galaxy M (see our Fig. 1 and Table 2) a comparable system. We must point out however that the comparison is based on a number of circumstantial evidences since there is only one galaxy redshift measured in the field and one does not really know whether galaxy M is physically bound to HRG 2302. Their piojected separation and sizes though are consistent with the assumption. Also, the magnitude difference between Cartwheel and G3 is about the same as in HRG 2302 and M, $\Delta M_B = 1.7$ and 1.5 respectively. The linear separation in the least massive pair – at the redshift of HRG 2302 – is scaled down with total luminosity as it would be expected for similar dynamical systems: the separation is 88 kpc in the Cartwheel-G3 pair (Higdon 1996) and 38 kpc in HRG 2302-M. Thus we have a case where a detailed mapping in the 21-cm line of neutral hydrogen would be highly desirable (project for a 21-cm line imaging of the HRG 2302 region underway). The role of regions I, II and III should be readdressed here as well. We identify regions I and II as the disturbed nuclear region of the target disk galaxy, and region III as a more massive and active H II cloud along the ring.

6. Conclusions

In this article we present the results of CCD surface photometry and a preliminary spectroscopy for the system HRG 2302 which is studied for the first time in the literature. The accuracy of this work's photometry is better than 0.06 mag in all passbands.

The main results and conclusions of the present work are: (a) HRG 2302 is probably an interacting Ring Galaxy, (b) it has been assigned the type of Elliptical-Knotted, based on FAOA (and as opposed to their previous classification of Polar Ring), (c) its spectrum is characteristic of H II regions, (d) several substructures have been revealed, which suggest the favored scenario of an intruder having collided with a face-on disk galaxy, (e) detailed surface photometry and spectroscopy help disen-

Table 5. Estimated dimensions (major and minor axes) of the substructures. "Outer" is a lower limit for the diameter of HRG 2302, as measured on the radial intensity profile, at 10% of the sky level in the R filter. The knots are shown in Fig. 9.

region	2a		2b		knot	2a		2b	
	″	kpc	″	kpc		″	kpc	″	kpc
outer	30.0	12.5	–	–	1	2.1	0.87	–	–
ring	13.2	5.5	–	–	2	2.1	0.87	–	–
I	2.7	1.1	2.0	0.83	3	3.4	1.4	2.2	0.91
II	3.0	1.2	1.5	0.63	4	2.7	1.1	–	–
I+II	7.3	3.0	3.5	1.5	5	4.5	1.9	–	–
III	4.1	1.7	3.0	1.2	6	2.4	1.0	–	–
					7	3.2	1.3	–	–

tangle the morphological details which may lead to a better classification and pRG family understanding, (f) two alternative scenarios for the formation of the HRG 2302 system are presented, (g) for the first time, at least 15 non-stellar objects, all probably (some certainly) galaxies, have been revealed within $4'$ around HRG 2302.

A detailed study of the rich field of galaxies around HRG 2302 is now in progress.

Acknowledgements. This work was partially supported by FAPEMIG grant CEX 1864/95, CNPq, FINEP, and CAPES (Brazilian institutions). This research has made use of the NASA/IPAC Extragalactic Database (NED, operated by the Jet Propulsion Laboratory, Caltech, under contract with NASA) and of the SIMBAD data base (operated by the CDS, Strasbourg, France). The help of the LNA staff at OPD is gratefully acknowledged. We gratefully thank Dr. Bo Reipurth for a critical reading of the manuscript. We thank an anonymous referee for relevant comments which improved the presentation of this work.

References

Appleton, P.N., Marcum, P.M., 1993, ApJ, 417, 90
Appleton, P.N., Marston, A.P., 1997, AJ, 113, 201
Appleton, P.N., Struck-Marcell, C., 1987, ApJ, 312, 566
Appleton P.N., Struck-Marcell C., 1996, in *Fundamentals of Cosmic Physics* 16/2, 111
Athanassoula E., Puerari I., Bosma A., 1997, MNRAS 286, 284
Baldwin J.A., Stone R.P.S., 1984, MNRAS 206, 241
Bekki K., 1997, ApJ 490, L37
Bekki K., 1998, ApJ 499, 635
Bessel M., 1990, PASP 102, 1181
Bransford, M.A., Appleton, P.N., Marston, A.P., Chamandaris, V., 1998, ApJ 116, 2757
Buat V., Deharveng J., Donas J., 1989, A&A 223, 42
Buta R., 1995, ApJS 96, 39
de Vaucouleurs G., 1948, Ann. d'Ap 11, 247
Dennefeld M., Materne J., 1980, The ESO Messenger 21, 29
Elmegreen D.M., 1998, Galaxies and Galactic Structure, Prentice-Hall, New Jersey, chapter 10
Faúndez-Abans M., Oliveira-Abans M., 1998a, A&AS 129, 357 (FAOA)
Faúndez-Abans M., Oliveira-Abans M., 1998b, A&AS 128, 289
Faúndez-Abans M., Oliveira-Abans M., Mennickent, R., 1999 (in preparation)
Faúndez-Abans M., Hertling P.G., Ramírez A.C., 1992, A&AS 94, 245
Ferrarese L., Mould J.R., Kennicutt Jr. R.C., Huchra J., Ford H.C., Freedman W.L., Stetson P.B., Madore B.F., Sakai S., Gibson B.K., Graham J.A., Hughes S.M., Illingworth G.D., Kelson D.D., Macri L., Sebo K., Silbermann N.A., 1999, AJ, in press (astro-ph/9908192)
Fosbury R.A.E., Hawarden T.G., 1977, MNRAS 178, 473
Gullixson C.A., 1992, in Astronomical CCD Observing and Reduction Techniques, PASPC 23, 130
Hamuy M., Walker A.R., Suntzeff N.B., Gigoux P., Heathcote S.R., Phillips M.M,, 1992, PASP 104, 533
Hamuy M., Suntzeff N.B., Heathcote S.R., Walker A.R., Gigoux P., Phillips M.M., 1994, PASP 106, 566
Higdon J.L., 1996, ApJ 467, 241
Keel W.C., Kennicutt R.C., Hummel E., van der Hulst J.M. 1985, AJ 90, 708
Kennicutt R.C., Roettiger K.A., Keel W.C., van der Hulst J.M., Hummel E., 1987, AJ 93, 1011
Landolt A.U., 1992, AJ 104, 340
Lynds R., Toomre A., 1976, ApJ 209, 382
Marston A.P., Appleton P.N., 1995, AJ 109, 1002
Poulain P., Nieto J.-L., 1994, A&AS 103, 573
Reshetnikov V.P., Hagen-Thorn V.A., Yakovleva V.A., 1994, A&A 290, 693
Reshetnikov V.P., Hagen-Thorn V.A., Yakovleva V.A., 1995, A&A 303, 398
Reshetnikov V.P., Hagen-Thorn V.A., Yakovleva V.A., 1996, A&A 314, 729
Roberts W.W, Huntley J.M., van Albada G.D., 1979, ApJ 233, 67
Rodríguez Espinosa, J.M., Stanga, R.M., 1990, ApJ, 365, 502
Sakamoto K., Okumura S.K., Ishizuki S., Scoville N.Z., 1999, preprint (astro-ph/9906454)
Sandage A., 1986, A&A 161, 89
Theys J.C., Spiegel E.A., 1976, ApJ 208, 650
Theys J.C., Spiegel E.A., 1977, ApJ 212, 616
Toomre A., 1978, IAU Symp. 79, 109
Whitmore B.C., Lucas R.A., McElroy D.B., Steiman-Cameron T.Y., Sackett P.D., Olling R.P., 1990, AJ 100, 1489
Young J., Allen L., Kenney J., Hesser A., Rownd B., 1996, AJ 112, 1903